Bidirectional DC–DC Wireless Power Transfer Based on LCC-C Resonant Compensation

Hurng-Liahng Jou, *Member, IEEE*, Jinn-Chang Wu, *Member, IEEE*, Kuen-Der Wu, and Chao-Yu Kuo

***Abstract*—A bidirectional dc–dc wireless power transfer (WPT) based on LCC-C resonance compensation is proposed in this article. For the power flowing from the primary side to the secondary side (P2S), the voltage source is converted to a current source (V–C) on the primary side and the current source is converted to a voltage source (C–V) on the secondary side. For the power flowing from the secondary side to the primary side (S2P), the V–C conversion occurs on the secondary side and the C–V conversion occurs on the primary side. The proposed bidirectional dc–dc WPT using LCC-C resonance compensation exhibits several advantages: 1) it operates in bidirectional power flow; 2) it prevents burn out of the coil when there is an open circuit on the load side or the coils are misaligned; and 3) it outputs a constant current (CC) or a constant voltage (CV). A hardware prototype is designed using the specification SAE-J2954, the operating frequency is 85 kHz, the maximum output power is 3.7 kW and the vertical distance for the coil gap is 15 cm. The experimental results verify that the proposed bidirectional dc–dc WPT performs as expected.**

***Index Terms*—Bidirectional power flow, dc–dc, misalignment, resonance compensation, wireless power transfer (WPT).**

I. Introduction

BECAUSE of air pollution, climate change and oil crises in the last century worldwide, many countries are studying alternatives to petrochemical fuel vehicles [1], [2]. Many plug-in hybrid vehicles (PHEVs) and pure battery electric vehicles (BEVs) are commercially available. Most charging systems for BEVs currently use the unidirectional power flow [3]–[6]. However, electricity prices are expected to change in a short time due to the development of smart grid [7], [8]. Studies are being conducted to connect the vehicle to the grid (V2G) [9], [10]. The V2G concept uses the battery of BEVs as an energy storage system to regulate the supply and the demand for the power grid and to allow smart grid demand management. Hence, the bidirectional power flow for charging systems of BEVs will be the trend.

Wireless power transfer (WPT) technology has four categories: magnetic field, electric wave, electric field, and other physical properties [11]. Currently, the development focuses on the energy transfer through a magnetic field. It uses magnetic induction [12] and magnetic resonance [13]. If a magnetic field is used to transfer energy for electrical vehicle applications, the transmitting (primary) coil must be buried in the ground. As a result, it requires less space and the system is convenient and not susceptible to metal shock or weather [14]. Magnetic induction WPT works based on the basic transformer principle that two power systems are coupled by two electrical coils (transmitting coil and receiving coil) placed very close to each other [15]. However, the coupling coefficient of magnetic induction WPT is lower than that of a conventional transformer because of the air coupling. Increasing coupling coefficient, shortening the distance between the transmitting coil and the receiving coil, avoiding misalignment, and using the proper circuit topologies can improve power transfer efficiency and reduces losses. Magnetic resonance WPT consists of a transmission coil, a primary resonance coil, a secondary resonance coil, and a receiving coil [13]. The resonance frequency of resonance coil is the same as the current frequency of transmission coil. The power is transmitted through the resonance of the resonance coil to the receiving coil. Magnetic resonance WPT has better advantages over magnetic induction WPT in terms of power transfer distance and directivity, but most magnetic resonance WPT are operated in a higher switching frequency (MHz) [16], [17]. Magnetic induction WPT using a lower switching frequency (kHz) transfers power over a shorter distance than the magnetic resonance WPT [18]. Besides, magnetic induction WPT is strictly directional, but a BEV can use wireless vertical charging to overcome this shortcoming. Magnetic induction WPT is also more efficient than magnetic resonance when the power transfer distance is short and the direction of power transfer is no misalignment. Hence, this study focuses on a wireless charger based on the principle of magnetic induction applied for charging the battery set of BEVs.

Magnetic induction WPT has an inherent magnetic leakage field, and it may cause unwanted electric and magnetic field (EMF) exposure and electromagnetic interference. For coexistence and electromagnetic compatibility (EMC) with electronic devices as well as to ensure safe operation in the condition of EMF exposure, the WPT system must comply with the related standards and regulatory requirements [19], [20].

Manuscript received April 7, 2020; accepted June 25, 2020. Date of publication June 29, 2020; date of current version September 22, 2020. This work was supported by ABLEREX Electronics Co., Ltd., Taiwan. Recommended for publication by Associate Editor P. Barbosa. *(Corresponding author: Hurng-Liahng Jou.)*

Hurng-Liahng Jou, Kuen-Der Wu, and Chao-Yu Kuo are with the Department of Electrical Engineering, National Kaohsiung University of Science and Technology, Kaohsiung 80778, Taiwan (e-mail: hljou5519@gmail.com; kuender@mail.ee.nkust.edu.tw; kuo.chaoyu@gmail.com).

Jinn-Chang Wu is with the Department of Microelectronics Engineering, National Kaohsiung University of Science and Technology, Kaohsiung 81157, Taiwan (e-mail: jinnwu@nkust.edu.tw).

This article has supplementary downloadable material available at https://ieeexplore.ieee.org, provided by the authors.

Color versions of one or more of the figures in this article are available online at https://ieeexplore.ieee.org.

Digital Object Identifier 10.1109/TPEL.2020.3005804

Wireless charging systems for BEVs are safer because WPT achieves energy transfer without contact. The transmitting coil and the receiving coil are electrically isolated. The conversion efficiency for a WPT system is increased if the coupling coefficient for the coupled coils is increased [21]. The coupling coefficient for a WPT system is lower than that of a conventional transformer, so there is significant imaginary impedance in the transmitting coil and the receiving coil. Hence, power is also transmitted less efficiently because there is an increase in reactive power. In order to reduce the effect of the imaginary impedance in the transmitting coil and the receiving coil, a conventional WPT system incorporates a resonance compensation capacitor to compensate for the reactive power on the transmitting coil and the receiving coil. The compensation capacitor does not change the impedance of the coil itself. After compensation, the apparent power in both the source side and the load side is reduced. Therefore, a conventional resonance compensation circuit for a WPT system includes four basic architectures [22]: SS, SP, PP, and PS. S and P represent series compensation and parallel compensation, respectively. The resonance frequency of P compensation for the primary side is affected by the magnitude of load if the capacitance of the parallel compensator capacitor is fixed [23]. Hence, P compensation for the primary side is not preferred. For primary side using S compensation, the primary coil current must be increased in order to maintain the output power when there is coil misalignment, so the current in the primary coil can become too large to cause burning. A position detection is necessary to address this shortcoming [3]. The current gain in the SP and SS resonance compensation circuits is inversely proportional to the coupling coefficient [24]. Hence, coil misalignment has a significant effect on the primary side using S compensation.

In order to improve the problems caused by the primary side using S compensation, LCC compensation architecture is used on the primary side [3]–[6], [25]. The LCC resonance compensation circuit on the primary side converts a voltage source via an inverter to a current source to produce a constant current in the primary coil and to prevent the overcurrent problem of primary side using S compensation [3], [4]. The LCC resonance compensation circuit on the secondary side outputs a constant current to the load. However, the output voltage increases when the load is light.

For conventional bidirectional WPT, the power flow direction and the magnitude of both real and reactive power flows are controlled by the relative phase angle and amplitude of the voltages generated by the full-bridge inverters of primary and secondary sides [26], [27]. The switching signals for the full-bridge inverters of primary and secondary sides should be synchronous to each other. This can be achieved by using a wireless communication interface between the controllers of primary and secondary sides. However, such solution will obviously increase the system cost and reduce its robustness. In [25], a control method uses active and reactive power generated by the full-bridge inverter of secondary side to perform synchronization between the primary and secondary sides without any wireless communications for controlling power transfer. However, real and reactive power flows are still controlled by the relative phase angle and magnitude of the voltages generated by the full-bridge inverters of primary and secondary sides. In general, the real and reactive power flows are also affected by the parameters of passive elements. Hence, the accuracy of power control is difficult because the phase is difficult to control accurately and the parameters of passive components will be varied due to the tolerance, age, and temperature.

This article proposes a bidirectional dc–dc WPT based on LCC-C resonance compensation. The major contributions of proposed bidirectional dc–dc WPT are as follows.

1) LCC-C resonance compensation is adopted to prevent burnt out of the coil when there is an open circuit on the load side or the coils are misaligned.
2) The control circuit is simplified because the control for performing constant current (CC)/constant voltage (CV) to charge the battery in grid to vehicle application and constant voltage in vehicle to grid application are implemented by the bidirectional buck/boost converter.
3) The synchronization between the primary and secondary side is not required.
4) The effect due to the parameter variation of the passive components can be solved by controlling the bidirectional buck/boost converter.
5) The bidirectional dc–dc WPT based on LCC-C resonance compensation is analyzed in detail.

A hardware prototype is developed and tested to validate its performance.

II. Circuit Topology

The architecture of LCC-C resonant compensation is extended from the S-S compensation architecture, and the LCC resonance compensation replaces C compensation in the primary side as well as the secondary side uses a series C resonance compensation circuit. In the power flow of primary to secondary (P2S), the voltage source is converted to a current source (V–C) on the primary side and the current source is converted to a voltage source (C–V) on the secondary side [28]. In the power flow of secondary to primary (S2P), the V–C conversion occurs on the secondary side and the C–V conversion occurs on the primary side. This feature allows the output of a bidirectional dc–dc WPT to be a voltage source regardless the direction of the power flow and prevents open circuit to damage the power converters on both sides.

The circuit topology for the proposed bidirectional dc–dc WPT using LCC-C resonance compensation is shown in Fig. 1. The circuit is composed of two full-bridge converters, an LCC-C resonance compensation circuit, a pair of coils, and a bidirectional buck/boost converter. The bidirectional buck/boost converter can be separately operated as a boost converter or a buck converter in different power flow direction. In the power flow of P2S, the primary side full-bridge converter converts the input dc voltage into a square voltage with a frequency of 85 kHz and then supplies to the LCC-C resonance compensation circuit. The output from the LCC-C resonance compensation circuit is rectified by the secondary side full-bridge converter to supply a dc voltage, and then the bidirectional buck/boost converter

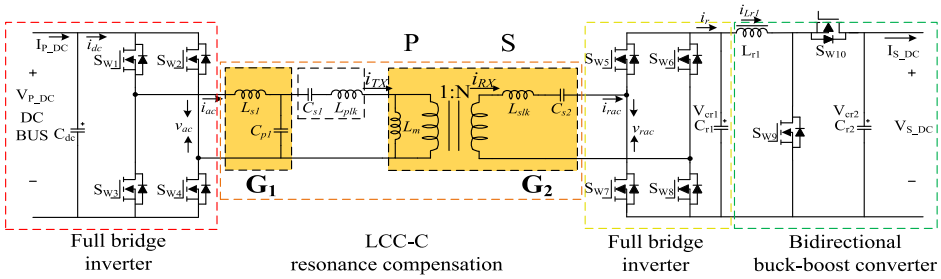

Fig. 1. Circuit topology for the proposed LCC-C bidirectional dc–dc WPT that uses LCC-C resonance compensation.

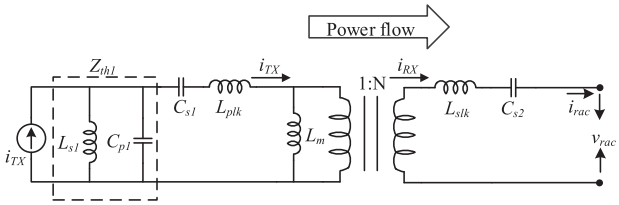

Fig. 2. Norton equivalent circuit for the V–C resonance compensation circuit.

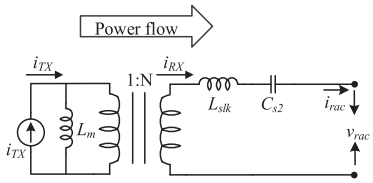

Fig. 3. Equivalent circuit for the LCC-C resonance compensation circuit.

operates in boost mode to convert this dc voltage to a regulated dc voltage/current. In the power flow of S2P, the bidirectional buck/boost converter operates in buck mode to generate the dc bus voltage for the secondary side full-bridge converter and then outputs a square voltage with a frequency of 85 kHz to the LCC-C resonance compensation circuit. The output from the LCC-C resonance compensation circuit is rectified by the full bridge of the primary side to obtain a constant dc voltage.

III. Power Flow of P2S

In the power flow of P2S, the dc voltage source on the primary side is converted to a square voltage v_{ac} by the full-bridge converter. The square voltage v_{ac} is sent to the LCC-C resonance compensation circuit. The resonance compensation circuit on the primary side is composed of L_{s1} and C_{p1} and this forms a V–C resonance compensation circuit with gain G_1. C_{s1} and L_{plk} are connected in series to form a series resonance compensation circuit and the output from this series resonance compensation circuit is connected to the primary coil, L_m. L_{slk} and C_{s2} form a C–V resonance compensation circuit with gain G_2. The turn ratio for the transformer is N. The voltage source v_{ac} and inductor L_{s1} can be replaced by a Norton equivalent, as shown in Fig. 2.

The Norton equivalent current can be represented as

$$i_{TX} = v_{ac} \times \frac{1}{Z_{L_{s1}}}. \tag{1}$$

As seen in Fig. 2, the parallel circuit L_{s1} and C_{p1} can be considered as the source impedance for i_{TX}. Its impedance is written as

$$Z_{th1} = \mathrm{Z}_{Ls1} // \mathrm{Z}_{Cp1} = \frac{Z_{Ls1} Z_{Cp1}}{Z_{Ls1} + Z_{Cp1}}. \tag{2}$$

For an ideal current source, Zth must be as large as possible, so L_{s1} and C_{p1} must be resonant, and C_{p1} can be derived as

$$C_{p1} = \frac{1}{\omega^2 L_{s1}}. \tag{3}$$

Hence, L_{s1} and C_{p1}can be regarded as open circuit. Because C_{s1} and L_{plk} are connected to the Norton equivalent current in series, it can be ignored. Therefore, the LCC-C resonant compensation circuit is equivalent to the circuit in Fig. 3. Accordingly, the gain for the V–C resonance compensation circuit G_1 can be written as

$$G_1 = \frac{1}{Z_{L_{s1}}} \tag{4}$$

where $Z_{L_{s1}}$ is the impedance of L_{s1}.

i_{TX} and L_m in Fig. 3 are transferred to the secondary side of the transformer and are replaced by a Thevenin equivalent circuit. Then, $L_m{}'$ can be written as

$$L_m{}' = \mathrm{N}^2 L_m. \tag{5}$$

The gain of C–V resonance compensation circuit G_2 can be written as

$$G_2 = Z_{L_m}{}'. \tag{6}$$

The LCC-C resonant compensation circuit is equivalent to the circuit in Fig. 4, where $L_m{}'$ and v_{eq1} are represented as

$$v_{eq1} = i_{TX} \times Z_{L_m}{}'. \tag{7}$$

As seen in Fig. 4, the series equivalent impedance for $L_m{}'$, L_{slk}, and C_{s2} must be as small as possible for an ideal voltage source, so $L_m{}'$, L_{slk}, and C_{s2} must be resonant. As a result, v_{rac} will approach v_{eq1}, and C_{s2} can be derived as

$$C_{s2} = \frac{1}{\omega^2 \left(L_{slk} + L_m{}'\right)}. \tag{8}$$

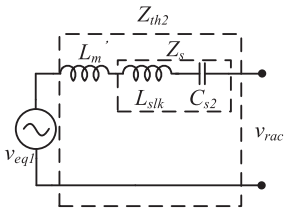

Fig. 4. Thevenin equivalent circuit for the C–V resonance compensation circuit.

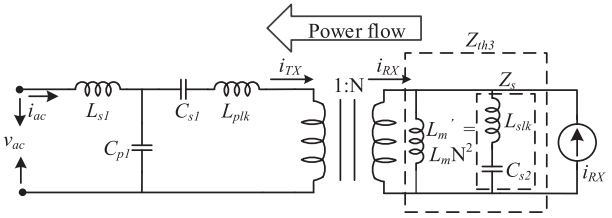

Fig. 5. Norton equivalent circuit for the V–C resonance compensation circuit.

The voltage gain G_{res_fw} from the primary side ac side voltage v_{ac} to the secondary side ac side voltage v_{rac} is written as

$$G_{res\_fw} = \frac{v_{rac}}{v_{ac}} = \mathrm{G_1} \times \frac{1}{\mathrm{N}} \times \mathrm{G_2} = \frac{1}{Z_{L_{s1}}} \times \frac{1}{\mathrm{N}} \times Z_{L_m}{}'. \tag{9}$$

The full-bridge converter on the secondary side operates as a rectifier and the bidirectional buck/boost converter operates as a boost converter. $\mathrm{V_{cr1}}$ is the voltage of $\mathrm{C_{r1}}$, and $\mathrm{V_{cr2}}$ is the voltage of $\mathrm{C_{r2}}$. If the boost converter operates in continuous-conduction mode (CCM), the duty ratio for the boost converter is written as

$$\mathrm{D} = \frac{\mathrm{V_{cr2}} - \mathrm{V_{cr1}}}{\mathrm{V_{cr2}}}. \tag{10}$$

IV. Power Flow of S2P

In the power flow of S2P, the bidirectional buck/boost converter operates as a buck converter. If the buck converter operates in CCM, the duty ratio for the buck converter is written as

$$\mathrm{D} = \frac{\mathrm{V_{cr1}}}{\mathrm{V_{cr2}}}. \tag{11}$$

L_m, L_{slk}, and C_{s2} in the LCC-C resonance compensation circuit operate as a V–C resonance compensation circuit, C_{s1}, L_{plk} in the LCC-C resonance compensation circuit operate as a series resonance compensation circuit, C_{p1} and L_{s1} in the LCC-C resonance compensation circuit operate as a C–V resonance compensation circuit.

The dc voltage source $\mathrm{V_{cr1}}$ is converted to a square voltage v_{rac} by the secondary side full-bridge converter. The voltage source, v_{rac}, and the impedance of L_{slk} and C_{s2} can be replaced by a Norton equivalent circuit shown in Fig. 5. The impedance of L_{slk} and C_{s2} can be represented as

$$Z_s = Z_{Cs2} + Z_{slk} = -\frac{1}{2\pi f C_{s2}} + 2\pi f L_{slk}. \tag{12}$$

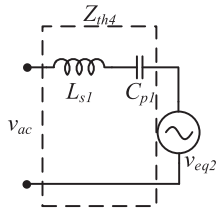

Fig. 6. Thevenin equivalent circuit for a C–V resonance compensation circuit.

i_{RX} can be represented as

$$i_{RX} = \frac{v_{rac}}{Z_s}. \tag{13}$$

In Fig. 5, the parallel circuit for $L_m{}'$ and Z_s can be regarded as the output impedance for current source i_{RX}, which is written as

$$Z_{th3} = \frac{Z_s \times Z_{Lm}{}'}{Z_s + Z_{Lm}{}'}. \tag{14}$$

Z_s and $Z_{Lm}{}'$ are resonant, so Z_{th3} is infinite and i_{RX} can be regarded as an ideal current source.

The current in the primary coil i_{TX} can be written as

$$i_{TX} = i_{RX} \times \mathrm{N}. \tag{15}$$

Since C_{s1} and L_{plk} operate as a series resonant circuit, their equivalent impedance is almost zero. Therefore, i_{TX} is connected to C_{p1} in parallel. Finally, i_{TX} and C_{p1} can be replaced by a Thevenin equivalent circuit and the LCC-C resonance compensation circuit can be simplified as Fig. 6, where v_{eq2} can be represented as

$$v_{eq2} = \frac{i_{TX}}{Z_{C_{p1}}} \tag{16}$$

where $Z_{C_{p1}}$ is the impedance of C_{p1}. Since L_{s1} and C_{p1} operate as a series resonant circuit, v_{ac} will approach v_{eq2}. The voltage gain G_{res_bw} from the secondary ac side voltage v_{rac} to the primary side ac side voltage v_{ac} is written as

$$G_{res\_bw} = \frac{v_{ac}}{v_{rac}} = \frac{1}{Z_s} \times \mathrm{N} \times \frac{1}{Z_{C_{p1}}}. \tag{17}$$

V. Control of Bidirectional DC–DC WPT

When the proposed bidirectional dc–dc WPT operates in the power flow of P2S, the power electronic switches of primary side full-bridge converter are switched to operate in the inverter mode and output a square wave, and the power electronic switches of secondary side full-bridge inverter maintain off to operate in the rectification mode. When the proposed bidirectional dc–dc WPT operates in the power flow of S2P, the power electronic switches of primary side full-bridge inverter maintain off to operate in the rectification mode, and the power electronic switches of secondary side full-bridge inverter are switched to operate in the inverter mode and output a square wave. Thus, the high-frequency synchronous signals for both full-bridge inverters are not necessary. Hence, a wireless communication interface

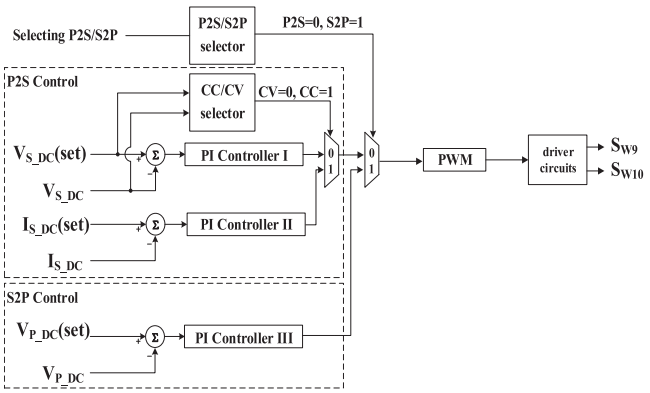

Fig. 7. Control block of the bidirectional buck/boost converter the proposed bidirectional dc–dc WPT.

between the primary and secondary sides can be avoided to increase the robustness of proposed bidirectional dc–dc WPT. In addition, the controls of both full-bridge inverters are simplified.

The bidirectional buck/boost converter is used to control the charging voltage/charging current for the battery in the power flow of P2S and the voltage of dc bus in the power flow of S2P. Fig. 7 is the control block of the bidirectional buck/boost converter in the proposed bidirectional dc–dc WPT. The operation of P2S and S2P power flow modes are selected through the P2S/S2P selector. When P2S is selected, the control object is the charging voltage ($\mathrm{V_{S\_DC}}$) or the charging current ($\mathrm{I_{S\_DC}}$) of battery set to perform CV or CC charging. The CV/CC charging is determined by comparing the charging voltage ($\mathrm{V_{S\_DC}}$) and the setting voltage $\mathrm{V_{S\_DC(set)}}$. The bidirectional buck/boost converter performs the CC charging when the charging voltage ($\mathrm{V_{S\_DC}}$) is lower than the setting voltage $\mathrm{V_{S\_DC(set)}}$. The bidirectional buck/boost converter performs the CV charging when the charging voltage ($\mathrm{V_{S\_DC}}$) is equal to the setting voltage $\mathrm{V_{S\_DC(set)}}$. When S2P is selected, the control object is the dc bus voltage ($\mathrm{V_{P\_DC}}$) of primary side full-bridge inverter.

For reducing the switching power loss of full-bridge inverters, the resonant frequency of LCC-C resonance compensation is designed to be slightly away from the switching frequency of full-bridge inverters to perform the inductive characteristic. The voltage gains G_{res_fw} and G_{res_bw} will be slightly affected due to the mismatch between the switching frequency and resonant frequency. In addition, the parameters of LCC-C resonance compensation have errors in practical application, and it will also affect the voltage gains G_{res_fw} and G_{res_bw}. The close-loop control of bidirectional buck/boost converter may cover these errors of voltage gains G_{res_fw} and G_{res_bw} to regulate the voltage/current in the proposed bidirectional dc–dc WPT.

VI. Experimental Results

A hardware prototype was implemented to verify the feasibility of the proposed bidirectional dc–dc WPT. A digital signal processor TMDSDOCK28069 is used as the controller. The prototype conforms to SAE-J2954 code [29] for which the specifications are a transmission distance of 15 cm

TABLE I
Main Parameters for the Experimental Prototype

Circuit system parameters		
Components	Parameters	Remarks
$\mathrm{V_{P\_DC}}$	400V	
$\mathrm{V_{S\_DC}}$	255V~403V	
Output power	3700W	
Full bridge inverter		
$\mathrm{S_{w1}}$~$\mathrm{S_{w8}}$	C3M0065090	Operational frequency 85 kHz
$\mathrm{C_{dc}}$	100uF	
$\mathrm{C_{r1}}$	150uF	
LCC-C Resonance Compensation		
L_{s1}	76.88uH	
C_{p1}	46nF	5S×5P
C_{s1}	35.03nF	4S× 3P
L_{plk}	98.29uH	
L_m	61.27uH	
1 : N	1:0.7873	
L_{slk}	61.75uH	
C_{s2}	35.02nF	8S× 6P
capacitor type of C_{p1}, C_{s1}, C_{s2}	47nF	R76UN24704040J
Bidirectional buck/boost converter		
$\mathrm{S_{w9}}$~$\mathrm{S_{w10}}$	C3M0065090	switching frequency 21.25kHz
$\mathrm{L_{r1}}$	500uH	
$\mathrm{C_{r2}}$	200uH	

TABLE II
Parameters for the Primary and Secondary Coils

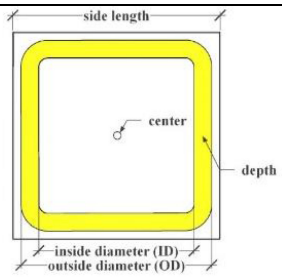

	Primary side	Secondary side
Side length	60cm	60cm
Inside diameter	34cm	38cm
Outside diameter	54cm	54cm
Depth	10cm	8cm

(WPT class S), a rated power of 3700 W (WPT class 1), and a switching frequency of 85 kHz. Table I shows the main parameters for the prototype, and Table II shows the parameters for the coupling coils.

For reducing the switching power loss of full-bridge inverters, the resonant frequency of LCC-C resonance compensation is designed to be slightly away from the switching frequency of full-bridge inverters to perform the inductive characteristic. The resonant frequency of L_{s1} and C_{p1} is 84.69 kHz, and it is slightly lower than 85 kHz. The resonant frequency of L'_m, L_{slk}, and C_{s2} is 85.1 kHz, and it is slightly higher than 85 kHz. Fig. 8 shows the bode plot for i_{ac} when the proposed bidirectional dc–dc WPT operates in the power flow of P2S under 0.38 coupling coefficient and 45-Ω load, and Fig. 9 shows the bode plots

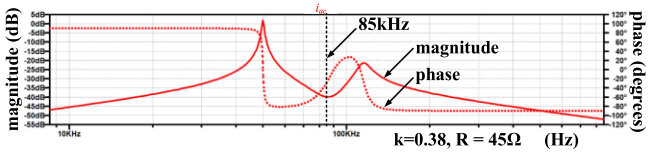

Fig. 8. Bode plot for i_{ac} of the proposed bidirectional dc–dc WPT in the power flow of P2S.

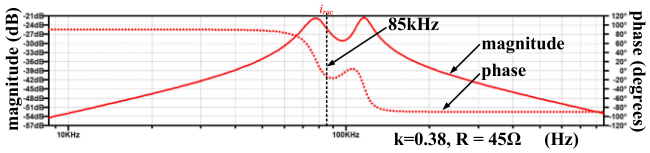

Fig. 9. Bode plot for $-i_{rac}$ of the proposed bidirectional dc–dc WPT in the power flow of S2P.

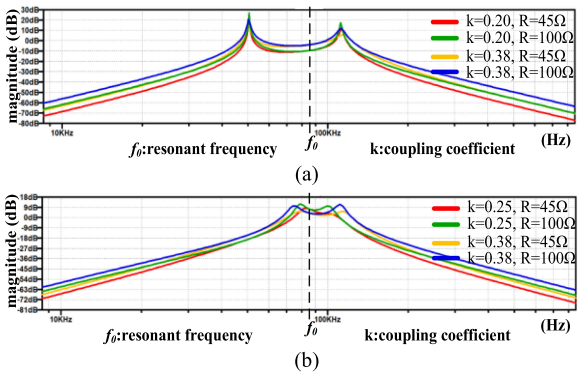

Fig. 10. Bode plots for the voltage gain of the proposed bidirectional dc–dc WPT with different coupling coefficients and different loads. (a) Power flow of P2S. (b) Power flow of S2P.

for $-i_{rac}$ when the proposed bidirectional dc–dc WPT operates in the power flow of S2P under 0.38 coupling coefficient and 45-Ω load. Figs. 8 and 9 verify that the proposed bidirectional dc–dc WPT can perform inductive characteristic to acquire zero voltage switching (ZVS) for the full-bridge power converter in the bidirectional power flow. However, the currents i_{ac} and $-i_{rac}$ increase slightly due to the existence of small inductive reactive power. Because the operation of the full-bridge inverters and the bidirectional buck/boost converter are decoupled by the capacitor $\mathrm{C_{r1}}$, the switching frequencies of full-bridge inverters and the bidirectional buck/boost converter are independent. For reducing the switching power loss, the switching frequency of bidirectional buck/boost converter is much less than that of full-bridge converters.

Fig. 10 shows bode plots for the voltage gain of the proposed bidirectional dc–dc WPT with different coupling coefficients and different loads. Fig. 10(a) shows the bode plot for P2S using (4), and Fig. 10(b) shows the bode plot for S2P using (12). Fig. 10(a) and (b) shows that the resonant frequency is almost independent of the coupling coefficient and the load. The voltage gain is almost unchanged at the switching frequency, so the proposed WPT can be operated as a voltage source in both power flows of P2S or S2P.

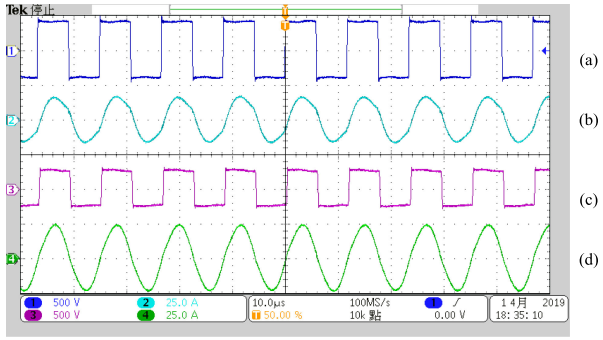

Fig. 11. Experimental results for the proposed bidirectional dc–dc WPT in the power flow of P2S under 3700 W. (a) v_{ac}. (b) i_{ac}. (c) v_{rac}. (d) i_{rac}.

The capacitance error of each capacitor in the prototype is 5%, and the inductor is wound by the laboratory of authors according to the design results. The resonant frequency of L_{s1} and C_{p1} is shifted from 84.69 to 81.95 kHz if the capacitance error is +5%, and the resonant frequency of L'_m, L_{slk}, and C_{s2} is shifted from 85.10 to 82.76 kHz if the capacitance error is +5%. The resonant frequency of L_{s1} and C_{p1} is shifted from 84.69 to 86 kHz if the capacitance error is −5%, and the resonant frequency of L'_m, L_{slk}, and C_{s2} is shifted from 85.10 to 86.99 kHz if the capacitance error is −5%. As can be seen in Fig. 10, it can be found that the gains are slightly decreased for power flows of P2S and S2P due to the 5% tolerance. The close-loop control of bidirectional buck/boost converter may cover these errors of voltage gains G_{res_fw} and G_{res_bw} to regulate the voltage/current. In addition, the tolerance will further push the resonant frequency of resonant compensation circuit away from the switching frequency and enlarge the reactive power to degrade the power efficiency. This problem can be overcome by changing the switching frequency to track the variation of resonant frequency due to the tolerances of components, and the authors will address this issue in the future research.

Fig. 11 shows the experimental results for the proposed bidirectional dc–dc WPT in the power flow of P2S, under 3700 W, respectively. Fig. 11(a) shows the ac voltage (v_{ac}) across the primary side full-bridge converter. The amplitude of v_{ac} is the input voltage $\mathrm{V_{P\_DC}}$. Fig. 11(b) shows the output current (i_{ac}) in the primary side full-bridge converter. As can be seen in Fig. 11 i_{ac} lags v_{ac}, which allows ZVS in the primary side full-bridge converter. The displacement power factor gradually increases as the load current is increased. Fig. 11(c) shows the waveforms for the ac voltage (v_{rac}) at the secondary side full-bridge converter. The amplitude of v_{rac} is the dc bus voltage $\mathrm{V_{cr1}}$ at the secondary side full-bridge converter and does not change with the load.

Fig. 12 shows the experimental results for the proposed bidirectional dc–dc WPT in the power flow of S2P under 3700 W, respectively. Fig. 12(a) shows the ac voltage (v_{ac}) at the primary side full-bridge converter. The amplitude of v_{ac} is the same as the dc bus voltage $\mathrm{V_{P\_DC}}$ on the primary side full-bridge converter. Fig. 12(b) shows the ac current (i_{ac}) in the primary side full-bridge converter. i_{ac} is out of the phase with v_{ac} for operation in the power flow of S2P and the amplitude of i_{ac} changes as the load is changed. Fig. 12(c) shows the ac voltage

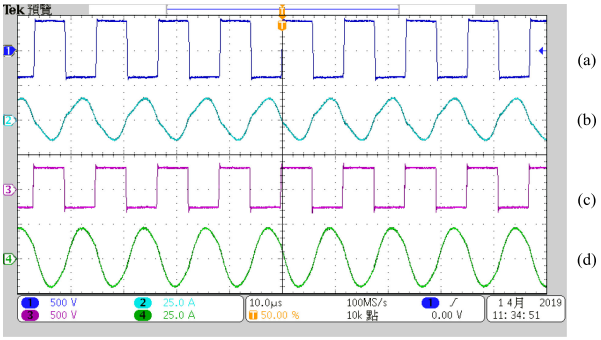

Fig. 12. Experimental results for the output power from the bidirectional dc–dc WPT in the power flow of S2P under of 3700 W. (a)v_{ac}. (b) i_{ac}. (c) v_{rac}. (d) i_{rac}.

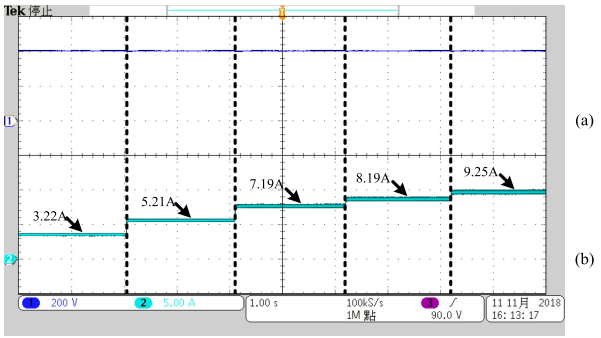

Fig. 13. Experimental results for the proposed bidirectional dc–dc WPT operating at CV in the power flow of P2S. (a) V_{S_DC}. (b) I_{S_DC}.

TABLE III
MEASURED EFFICIENCY OF Fig. 13

voltage(V)	current(A)	power(W)	Efficiency (%)
400	3.22	1288	93.07
400	5.21	2084	94.28
400	7.19	2876	94.11
400	8.19	3276	93.96
400	9.25	3700	93.86

(v_{rac}) on the secondary side full-bridge converter. The amplitude of v_{rac} is the same as the dc bus voltage V_{cr1} on the secondary side full-bridge converter. Fig. 12(d) shows the waveforms for the ac current (i_{rac}). It is seen that i_{rac} is inductive and lags v_{rac}, which allows ZVS in the secondary side full-bridge converter.

Fig. 13 shows the experimental results for the proposed bidirectional dc–dc WPT operating at CV in the power flow of P2S. It is seen that V_{S_DC} is almost unchanged at 400 V in Fig. 13(a) and I_{S_DC} in Fig. 13(b) exhibits a step change of 3.22, 5.21, 7.19, 8.19, and 9.25 A when there is a step change in the load. This means that the voltage is maintained as a constant value, regardless of the change in the output current. This verifies that the proposed system provides CV under different loads. Table III shows the measured efficiency of Fig. 13.

Fig. 14 shows the experimental results for the proposed bidirectional dc–dc WPT operating at CC in the power flow of P2S. It is seen that the output current I_{S_DC} is maintained at dc 6 A and the output voltage of V_{S_DC} exhibits a step change to 266,

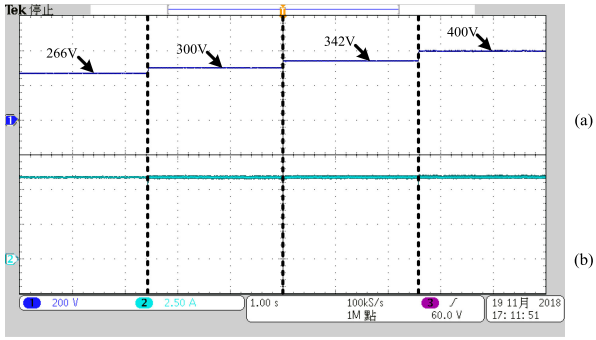

Fig. 14. Experimental results for the proposed bidirectional dc–dc WPT operating at CC in the power flow of P2S. (a) V_{S_DC}. (b) I_{S_DC}.

TABLE IV
MEASURED EFFICIENCY OF Fig. 14

voltage(V)	current(A)	power(W)	efficiency(%)
266	6	1596	93.57
300	6	1800	94.13
342	6	2052	94.28
400	6	2400	94.24

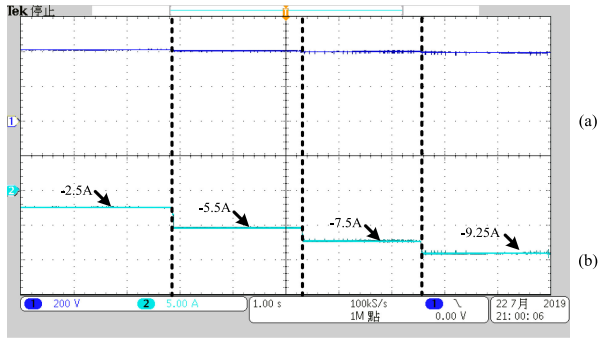

Fig. 15. Experimental results for the proposed bidirectional dc–dc WPT in the power flow of S2P. (a) V_{P_DC}. (b) I_{P_DC}.

300, 342, and 400 V when there is a step change in the load. This verifies that the proposed bidirectional dc–dc WPT in the power flow of P2S provides CC under different loads. Table IV shows the measured efficiency of Fig. 14.

Fig. 15 shows the experimental results for the proposed bidirectional dc–dc WPT in the power flow of S2P. It is seen that V_{P_DC} is almost unchanged at 400 V in Fig. 15(a) and I_{P_DC} in Fig. 15(b) exhibits a step change to -2.5, -5.5, -7.5, and -9.25 A when there is a step change in the load. The voltage is a constant value and the load current is changed, so the proposed bidirectional dc–dc WPT in the power flow of S2P can be realized for different levels of output power.

The dynamic characteristics of proposed bidirectional dc–dc WPT are shown in Fig. 13 for constant voltage application under load change in the power flow of P2S, in Fig. 14 for constant current application under load change in the power flow of P2S, and in Fig. 15 for constant voltage application under load change in the power flow of S2P. Figs. 13–15 verify that the proposed bidirectional dc–dc WPT have good dynamic performance in both P2S and S2P power flow.

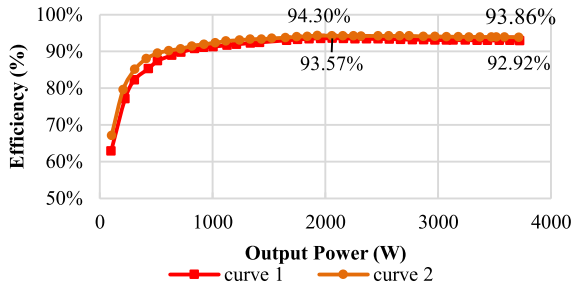

Fig. 16. Power efficiency for the proposed bidirectional dc–dc WPT in the power flow of P2S.

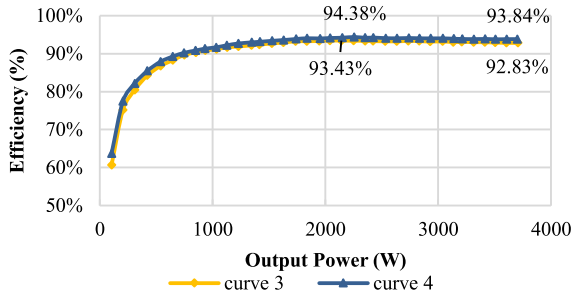

Fig. 17. Power efficiency for the proposed bidirectional dc–dc WPT in the power flow of S2P.

Figs. 16 and 17 show the power efficiency of the proposed bidirectional dc–dc WPT in the power flow of P2S and S2P. A Yokogawa WT1600 is used for measurement. The working power for the control circuit is ignored when measuring the power efficiency. In the power flow of P2S, the power efficiency measurement condition is set at 400 V for both $\mathbf{V_{P\_DC}}$ and $\mathbf{V_{S\_DC}}$, and the output current is changed by the adjustable load to measure the power efficiency. In the power flow of S2P, the power efficiency measurement condition is also set at 400 V for both $\mathbf{V_{S\_DC}}$ and $\mathbf{V_{P\_DC}}$, and the output current is changed by adjustable load to measure power efficiency.

Curve 1 in Fig. 16 shows the power efficiency for the proposed bidirectional dc–dc WPT in the power flow of P2S using a ferrite core in $\boldsymbol{L_{s1}}$. The maximum power efficiency is 93.57% at 2050 W. The power efficiency for a full load is 92.92%. Curve 2 shows the power efficiency using an air core in $\boldsymbol{L_{s1}}$. The maximum power efficiency is 94.30% at 1950 W and the power efficiency is 93.86% for a full load.

Curve 3 in Fig. 17 shows the power efficiency for the proposed bidirectional dc–dc WPT in the power flow of S2P using a ferrite core in $\boldsymbol{L_{s1}}$. The maximum power efficiency is 93.43% at 2040 W. The power efficiency at full load is 92.83%. Curve 4 shows the power efficiency using an air core in $\boldsymbol{L_{s1}}$. The maximum power efficiency is 94.38% at 2250 W and the power efficiency is 93.84% at full load.

As seen in Figs. 16 and 17, the power efficiency using an air core is greater than that using a ferrite core in $\boldsymbol{L_{s1}}$.

To verify the effect of misalignment of coils and the vertical or horizontal offset on the coupling coefficient and transmission efficiency for the proposed bidirectional dc–dc WPT, the primary coil and secondary coils were mounted on square acrylic plate

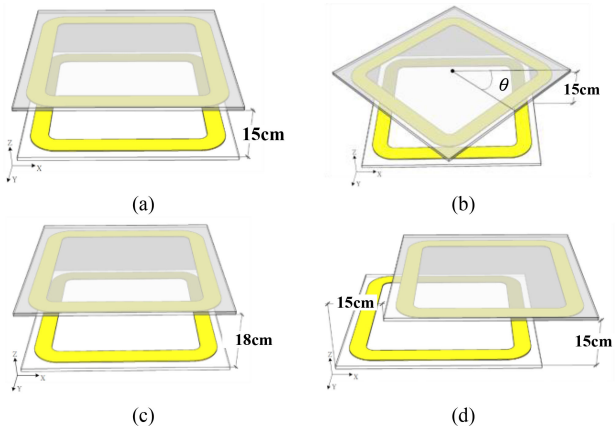

Fig. 18. Misalignment between two coils. (a) No misalignment. (b) Rotational misalignment. (c) Vertical misalignment. (d) Horizontal misalignment.

TABLE V
MEASURED RESULTS FOR COIL PARAMETERS UNDER MISALIGNMENT

Parameter	Case 1	Case 2	Case 3	Case 4
L_{p_open}	161.46uH	159.48uH	155.36uH	160.46uH
L_{p_close}	136.37uH	137.48uH	140.02uH	150.33uH
L_{s_open}	99.47uH	99.49uH	95.78uH	98.98uH
$L_{s\ close}$	83.43uH	86.09uH	86.53uH	92.74uH
Coupling coefficient	0.38	0.368	0.314	0.251
1 : N	0.7849	0.7898	0.7852	0.7854
L_{plk}	100.11uH	100.75uH	106.54uH	120.14uH
L_m	61.35uH	58.73uH	48.82uH	40.32uH
L_{slk}	61.67uH	62.85uH	65.68uH	74.11uH

of 60 × 60 cm. In the experiments, the coordinates of the coils are defined as (*X*, *Y*, *Z*) and the center point of primary coil is defined as (0, 0, 0). The experiments simulate four scenarios: No misalignment (case 1), rotational misalignment (case 2), vertical (*Z*-axis) misalignment (case 3), and horizontal (*X*-axis) misalignment (case 4). Fig. 18(a) shows the position of the coils for case 1. In this case, there is no misalignment between the primary and secondary coils, and the vertical distance between the two coils is 15 cm. The center point of the secondary coil is at coordinate (0, 0, 15). Fig. 18(b) shows the position of the coils for case 2. There is no misalignment along the *X*-axis, *Y*-axis, and *Z*-axis. However, the secondary coil is rotated 45° around the *X*-axis. The position of the coils for case 3 is shown in Fig. 18(c). There is no offset in the *X*-axis or *Y*-axis, but the vertical distance between the two coils is increased from 15 to 18 cm. Therefore, the center point of the secondary coil is at (0, 0, 18). The position of the coils for case 4 is shown in Fig. 18(d). Fig. 18(d) shows that the secondary coil is moved 15 cm along the *X*-axis, the *Y*-axis has no offset and the *Z*-axis is still 15 cm. Therefore, the center point of secondary coil is at (15, 0, 15). The frequency of the LCR meter is set at 85 kHz to measure the parameters of the coils. Table V shows the measured results, which are equivalent to the parameters for the transformer model.

Fig. 19 shows the relationship between conversion efficiency and the output power for the proposed bidirectional dc–dc WPT in the power flow of P2S under four misalignment scenarios. Fig. 19 shows that the power conversion efficiency is barely

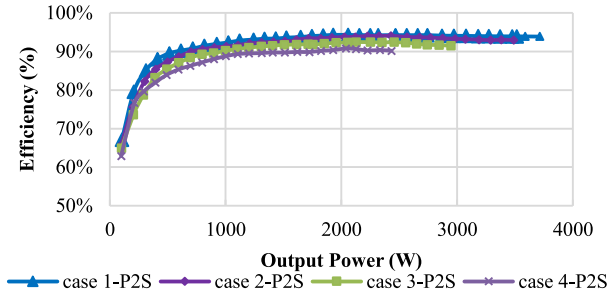

Fig. 19. Relationship between the conversion efficiency and the output power for the proposed bidirectional dc–dc WPT in the power flow of P2S.

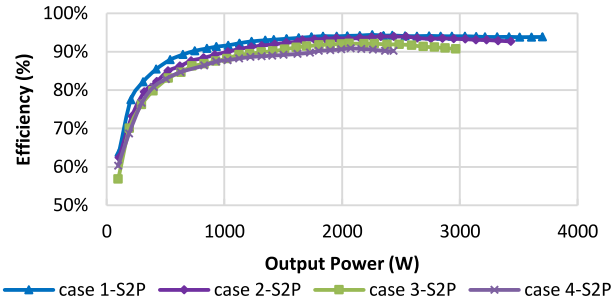

Fig. 20. Relationship between conversion efficiency and the output power for the proposed bidirectional dc–dc WPT in the power flow of S2P.

affected by misalignment, but power transmission is significantly affected. Therefore, misalignment affects the coupling coefficient between two coils, but does not affect the resonant frequency of the LCC-C resonance compensation circuit.

Fig. 20 shows the relationship between the conversion efficiency and the output power for the proposed bidirectional dc–dc WPT in the power flow of S2P under four misalignment scenarios. Fig. 20 shows that the power conversion efficiency is barely affected by misalignment, but power transmission is significantly affected. Therefore, misalignment affects the coupling coefficient between two coils, but does not affect the resonant frequency of the LCC-C resonance compensation circuit. Therefore, coil misalignment, vertical misalignment, or horizontal misalignment has little effect on the power conversion efficiency, but each has a significant effect on the power transmission in the power flows of P2S and S2P.

VII. Conclusion

The output current source creates a notable increase in the resonant tank voltage for the current source compensation of a WPT topology when the open circuit occurs due to the failure of output power converter or load. Therefore, more complicated control methods are required to achieve bidirectional WPT [24], [25]. This study develops a bidirectional dc–dc WPT based on LCC-C resonance compensation. and it has the following features.

1) The bidirectional dc–dc WPT is designed to have inductive characteristics so that the power electronics operate in ZVS. This decreases the switching loss in the power electronic switches.
2) The LCC-C resonance compensation circuit converts the voltage source into a current source and transmits it to the coil in either power flow of P2S or power flow of S2P. This prevents overcurrent of the coil when there is no load, or the coils are misaligned. Because the output is a voltage, the circuit does not produce an increasing current in the resonant tank voltage.
3) This topology uses fewer components than other current source compensation topologies [24], [25]. Hence, the transmission efficiency is increased.

References

[1] M. Guarnieri, "A lesson from past energy crises [Historical]," *IEEE Ind. Electron. Mag.*, vol. 10, no. 2, pp. 59–63, Jun. 2016.
[2] N. Sehgal and K. K. Pandey, "Aftermath of 2008 financial crisis on oil prices," in *Proc. 7th Int. Joint Conf. Knowl. Discovery, Knowl. Eng. Knowl. Manage.*, Lisbon, Portugal, 2015, pp. 235–240.
[3] L. Peng, L. Xiao-kun, G. Zhu, M. Xie, and X. Li, "Characteristics research on double LCC compensation converter in the inductive energy transfer system," in *Proc. Int. Conf. Ind. Inform. - Comput. Technol., Intell. Technol., Ind. Inf. Integration*, Wuhan, China, 2015, pp. 243–246.
[4] M. Khalilian and P. Guglielmi, "Primary-side control of a wireless power transfer system with double-sided LCC compensation topology for electric vehicle battery charging," in *Proc. IEEE Int. Telecommun. Energy Conf.*, Turin, Italy, 2018.
[5] W. Li, H. Zhao, T. Kan, and C. Mi, "Inter-operability considerations of the double-sided LCC compensated wireless charger for electric vehicle and plug-in hybrid electric vehicle applications," in *Proc. IEEE PELS Workshop Emerg. Technol. : Wireless Power*, Daejeon, South Korea, 2015.
[6] C. Chou, M. Tampubolon, J. Lin, Y. Hsieh, and H. Chiu, "Study on LCC-C wireless power transfer," in *Proc. IEEE Wireless Power Transfer Conf.*, Taipei, Taiwan, 2017.
[7] H. Yang, J. Zhang, J. Qiu, S. Zhang, M. Lai, and Z. Y. Dong, "A practical pricing approach to smart grid demand response based on load classification," *IEEE Trans. Smart Grid*, vol. 9, no. 1, pp. 179–190, Jan. 2018.
[8] E. Spanò, L. Niccolini, S. D. Pascoli, and G. Iannacconeluca, "Last-meter smart grid embedded in an Internet-of-Things platform," *IEEE Trans. Smart Grid*, vol. 6, no. 1, pp. 468–476, Jan. 2015.
[9] U. C. Chukwu and S. M. Mahajan, "Modeling of V2G net energy injection into the grid," in *Proc. 6th Int. Conf. Clean Elect. Power*, Santa Margherita Ligure, Italy, 2017, pp. 437–440.
[10] M. J. E. Alam, K. M. Muttaqi, and D. Sutanto, "Effective utilization of available PEV battery capacity for mitigation of solar PV impact and grid support with integrated V2G Functionality," *IEEE Trans. Smart Grid*, vol. 7, no. 3, pp. 1562–1571, May 2016.
[11] M. Yilmaz and P. T. Krein, "Review of battery charger topologies, charging power levels, and infrastructure for plug-in electric and hybrid vehicles," *IEEE Trans. Power Electron.*, vol. 28, no. 5, pp. 2151–2169, May 2013.
[12] X. Yin, X. Wang, and P. He, "Simulation analysis and research of magnetic coupling resonant wireless power transmission system," in *Proc. Int. Conf. Intell. Transp., Big Data & Smart City*, Xiamen, China, 2018, pp. 772–775.
[13] Y. Li, Q. Duan, and Y. Huang, "Topology and parameter optimization design for magnetic resonance wireless power transfer system," in *Proc. IEEE PELS Workshop Emerg. Technol. : Wireless Power Transfer*, Xiamen, China, 2017, pp. 111–116.
[14] S. Wang and D. G. Dorrell, "Loss analysis of circular wireless EV charging coupler," *IEEE Trans. Magn.*, vol. 50, no. 11, Nov. 2014, Art. no. 8402104.
[15] N. Chawla and S. Tosunoglu, "State of the art in inductive charging for electronic appliances and its future in transportation," in *Proc.Florida Conf. Recent Adv. Robot.*, May 10–11, 2012.
[16] S. Kim, I. K. Cho, J. I. Moon, S. I. Jeon, and J. I. Choi, "5W wireless power transmission system with coupled magnetic resonance," in *Proc. 5th IEEE Int. Symp. Microw., Antenna, Propag. EMC Technol. Wireless Commun.*, Chengdu, China, 2013, pp. 255–258.
[17] F. Jolani, Y. Yu, and Z. Chen, "A novel planar wireless power transfer system with strong coupled magnetic resonances," in *Proc. IEEE Int. Wireless Symp.*, 2014.
[18] I. Lee, N. Kim, I. Cho, and I. Hong, "Design of a patterned soft magnetic structure to reduce magnetic flux leakage of magnetic induction wireless power transfer systems," in *IEEE Trans. Electromagn. Compat.*, vol. 59, no. 6, pp. 1856–1863, Dec. 2017.

[19] S. Park, "Evaluation of electromagnetic exposure during 85 kHz wireless power transfer for electric vehicles," *IEEE Trans. Magn.*, vol. 54, no. 1, Jan. 2018, Art. no. 5100208.
[20] D. Kuerschner, G. Ombach, L. Percebon, and S. Mathar, "Magnetic leakage field study of a 7 kW wireless electric vehicle charging system," *World Electric Veh. J.*, vol. 8, pp. 501–510, 2016.
[21] M. Bojarski, E. Asa, K. Colak, and D. Czarkowski, "A 25 kW industrial prototype wireless electric vehicle charger," in *Proc. IEEE Appl. Power Electron. Conf. Expo.*, Long Beach, CA, USA, 2016, pp. 1756–1761.
[22] Y. H. Sohn, B. H. Choi, E. S. Lee, G. C. Lim, G. Cho, and C. T. Rim, "General unified analyses of two-capacitor inductive power transfer systems: Equivalence of current-source SS and SP compensations," *IEEE Trans. Power Electron.*, vol. 30, no. 11, pp. 6030–6045, Nov. 2015.
[23] C.-S. Wang, O. H. Stielau, and G. A. Covic, "Design considerations for a contactless electric vehicle battery charger," in *IEEE Trans. Ind. Electron.*, vol. 52, no. 5, pp. 1308–1314, Oct. 2005.
[24] J. Hou, Q. Chen, K. Yan, X. Ren, S. Wong, and C. K. Tse, "Analysis and control of S/SP compensation contactless resonant converter with constant voltage gain," in *Proc. IEEE Energy Convers. Congr. Expo.*, Denver, CO, USA, 2013, pp. 2552–2558.
[25] Y. Tang, Y. Chen, U. K. Madawala, D. J. Thrimawithana, and H. Ma, "A new controller for bidirectional wireless power transfer systems," *IEEE Trans. Power Electron.*, vol. 33, no. 10, pp. 9076–9087, Oct. 2018.
[26] L. Zhao, D. J. Thrimawithana, and U. K. Madawala, "Hybrid bidirectional wireless EV charging system tolerant to pad misalignment," *IEEE Trans. Ind. Electron.*, vol. 64, no. 9, pp. 7079–7086, Sep. 2017.
[27] T. Diekhans and R. W. De Doncker, "A dual-side controlled inductive power transfer system optimized for large coupling factor variations and partial load," *IEEE Trans. Power Electron.*, vol. 30, no. 11, pp. 6320–6328, Nov. 2015.
[28] W. Zhang and C. C. Mi, "Compensation topologies of high-power wireless power transfer systems," *IEEE Trans. Veh. Technol.*, vol. 65, no. 6, pp. 4768–4778, Jun. 2016.
[29] *Wireless Power Transfer for Light-Duty Plug-In/Electric Vehicles and Alignment Methodology*, J2954_201711, SAE International, May 23, 2019. [Online]. Available: https://www.sae.org/standards/content/j2954_201711/

Hurng-Liahng Jou (Member, IEEE) was born in Taiwan, R.O.C., in 1959. He received the B.S. degree from Chung Yuan University, Jonglih, Taiwan, in 1982, and the M.S. and Ph.D. degrees from the National Cheng Kung University, Tainan, Taiwan, in 1984 and 1991, respectively, all in electrical engineering.

He is currently working as a Professor with the Department of Electrical Engineering, National Kaohsiung University of Science and Technology, Kaohsiung, Taiwan. His current research interests include power electronics applications and power quality improvement techniques.

Jinn-Chang Wu (Member, IEEE) was born in Tainan, Taiwan, R.O.C., in 1968. He received the B.S. degree from the National Kaohsiung Institute of Technology, Kaohsiung, Taiwan, in 1988, and the M.S. and Ph.D. degrees in electrical engineering from the National Cheng Kung University, Tainan, Taiwan, in 1992 and 2000, respectively.

He is currently working as a Professor with the Department of Microelectronics Engineering, National Kaohsiung University of Science and Technology, Kaohsiung, Taiwan. His current research interests include power electronics applications and power quality improvement techniques.

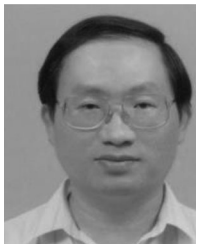

Kuen-Der Wu was born in Tainan, Taiwan, R.O.C., in 1954. He received the B.S. degree from Tamkang University, Taipei, Taiwan, in 1977, and the M.S. degree from the National Cheng Kung University, Tainan, Taiwan, in 1980, all in electrical engineering.

He is currently working as an Associate Professor with the Department of Electrical Engineering, National Kaohsiung University of Science and Technology, Kaohsiung, Taiwan. His current research interests include power electronics applications.

Chao-Yu Kuo was born in Tainan, Taiwan R.O.C. in 1992. He received the B.S. degree from the National Formosa University, Taiwan, in 2015, and the M.S. degree from the National Kaohsiung University of Science and Technology, Kaohsiung, Taiwan, in 2019, all in electrical engineering.

His current research interests include is power electronics applications.